Vietnam Journal of Science and Technology ***62*** *(2024)*

doi:10.15625/2525-2518/18571

Numerical simulation and experimental study on effect of cooling rate on microstructure and strength of nanostructured materials

Nguyen Hong Hai[1], Le Minh Duc[2], Hoang Thi Ngoc Quyen[1], Pham Quang[1, *]

[1]*Faculty of Materials Engineering, School of Materials Science and Engineering, Hanoi University of Science and Technology, No.1 Dai Co Viet, Ha Noi, Viet Nam*

[2]*Department of Materials Science and Engineering, Faculty of Mechanical Engineering, Le Quy Don Technical University, No. 236 Hoang Quoc Viet, Ha Noi, Viet Nam*

[*]Emails: *quang.pham@hust.edu.vn*

Received: 23 July 2023; Accepted for publication: 15 April 2024

Abstract. In this study, by numerical simulation (finite element method, FEM) and experimental, the cooling rate was investigated by changing the product thickness (20, 3, 2, 1, 0.5 and 0.3) *mm* of Al based two-phase nanostructured materials casted through a copper mold. The effect of cooling rate on the microstructure and strength of the alloy was studied. The Experimental results showed that the precipitated intermetallic phases have a decreasing size corresponding to the increasing cooling rates by simulation from ~10^2 *K/s* to ~10^4 *K/s*. The results show that an appropriate cooling rate can improve the microstructure and properties of the alloy. The Abaqus/Standard capability for uncoupled heat transfer analysis was intended to model solid body heat conduction with general, temperature-dependent conductivity; internal energy (including latent heat effects); and quite general convection and radiation boundary conditions. This study describes the basic energy balance, constitutive models, boundary conditions, finite element discretization, and time integration procedures used. The time step used an automatic algorithm through the smallest tolerance. The maximum temperature change was allowed over a period and the increment was adjusted for this parameter, as was the rate of convergence in the non-linear cases. First-order heat transfer elements used the rule of numerical integration with integrated stations located at the corners of the element for thermal capacitance terms. (Jacobian terminology). This approach is particularly effective when there is a strong latent thermal effect. Thus, first - order elements were used in the case of latent heat. The HEATCAP element is available for single - point pooled thermal capacitance modeling. Centralized film loading options between the mold and the casting were specified by the user.

Keywords: Aluminium based, Al–Mn series, nanostructured, metallic glass, cooling rate, solidification, FEM simulation, Abaqus/Standard, uncoupled heat transfer analysis.

Classification numbers: 2.9.1, 4.10.4, 5.9.3.

1. INTRODUCTION

Generally, quasicrystals can be divided into aluminium-based, magnesium-based, and titanium-based. The Al base is the most widely studied, especially Al–Cu–Fe series and Al–Mn series. The added elements are cheap, easy to obtain, and non- toxic; they have become very popular. Meanwhile, Al–Mn alloy is also used widely due to the formation of part of the pure aluminium phase and to a certain extent to improve the brittleness of the alloy [1-3]. In the case of rheo-die casting technology (i.e.combination of rheocasting with die casting) the turbulent flow of metal under high pressure that involves a lot of gas, resulting in the presence of porosity in castings, is substituted by a laminar flow allowing more "peaceful" mold filling due to lower pouring temperature (between liquidus and solidus). In recent years, my research team has carried out by to produce a semi-solid structure of the globular primary alpha phase via continuous rheocasting and rheo-die casting [4 - 8].

In general, the preparation process of Al base cast alloys includes casting, solid solution and aging heat treatment. For cast aluminium alloys, increasing the cooling rate will decrease the size of α-Al grains and secondary/primary phases in the as-cast microstructure. The results show that an appropriate cooling rate can improve the microstructure and properties of the alloy [9-12]. As such, increasing cooling rate correlates with a higher degree of microstructural refinement, thus increasing the mechanical properties of alloys in the as-cast condition. For Al base cast alloys, the as-cast microstructure is destroyed by subsequent solution treatment. However, the Al–Mn alloy suffers from poor thermal stability and is in a sub-stable state. So researchers tried to further improve the stability of the alloy by adding transition group elements [13,14]. For example, the studies on the Al–Mn system were focused on the influence of alloying elements like Fe [15], Be [16], and Ce [17] on its microstructure and properties. However, the addition of a third or even multiple elements can be problematic; for example, the addition of Be increases the ability of I-phase nucleation in the alloy [18–20]. However, beryllium is known for being carcinogenic and causing other serious diseases such as berylliosis [21]. Thus, other elements that could enhance the I-phase formation during conventional casting processes are desirable. Cerium was reported to be an effective addition in improving the I-phase formation in Al–Mn alloys under different solidification conditions [22]; nonetheless, its effectiveness was recently disputed by Coury et al. [23]

Combined with related studies [24–27], the addition of Fe not only increases the thermal stability of the alloy but also increases the ability to form quasicrystalline phases, and Fe is cheap, readily available, and non-toxic. The effect of iron addition on the formed phases of the alloy has also been studied in the literature [28], but there are few systematic studies in the literature on the types, morphology, and thermal expansion properties of the formed phases of the alloy under different preparation processes.

In this study, by numerical simulation (ABAQUS, FEM) [29] and experimental methods, the cooling rate was investigated by changing the product thickness (0.3, 0.5, 1, 2, 3 and 20 *mm*) of Al based two-phase nanostructured materials casted through a copper mold. Simulation and Experimental results showed that the precipitated intermetallic phases have a decreasing size corresponding to the increasing cooling rates.

2. METHODOLOGY AND MODELING

The Abaqus/Standard capability for uncoupled heat transfer analysis is intended to model solid body heat conduction with general, temperature-dependent conductivity; internal energy (including latent heat effects); and quite general convection and radiation boundary conditions.

This study describes the basic energy balance, constitutive models, boundary conditions, finite element discretization, and time integration procedures used.[30]

2.1. The basic energy balance (Green and Naghdi)

$$\int_V \rho \dot{U} dV = \int_S q dS + \int_V r dV \tag{1}$$

where V is a volume of solid material, with surface area S; $\boldsymbol{\rho}$ is the density of the material; $\dot{\boldsymbol{U}}$ is the material time rate of the internal energy; q is the heat flux per unit area of the body, flowing into the body; and r is the heat supplied externally into the body per unit volume.

It is assumed that the thermal and mechanical problems are uncoupled in the sense that $\boldsymbol{U = U(T)}$ only, where $\boldsymbol{T}$ is the temperature of the material, and q and r do not depend on the strains or displacements of the body. For simplicity a Lagrangian description is assumed, so "volume" and "surface" mean the volume and surface in the reference configuration.

2.2. Specific heat, latent heat

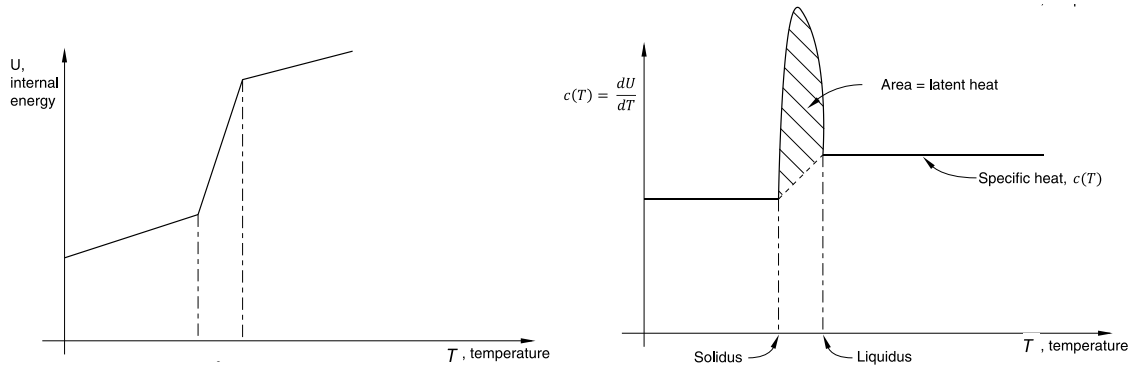

Figure 1. Specific heat, latent heat definition [30].

This relationship is usually written in terms of a specific heat, neglecting coupling between mechanical and thermal problems:

$$\boldsymbol{c(T) = \frac{dU}{dT}} \tag{2}$$

Except for latent heat effects at phase changes, which are given separately in terms of solidus and liquidus temperatures (the lower and upper temperature bounds of the phase change range) and the total internal energy associated with the phase change, called the latent heat. When latent heat is given, it is assumed to be in addition to the specific heat effect (see Figure 1). In many cases it is reasonable to assume that the phase change occurs within a known temperature range, which can be specified by the user. However, in some cases, it may be necessary to include a kinetic theory for the phase change to model the effect accurately.

Heat conduction is assumed to be governed by the Fourier law:

$$\boldsymbol{f = -k \frac{\partial T}{\partial x}} \tag{3}$$

where $k = k(T)$ is the conductivity matrix,; f is the heat flux; and x is position. The conductivity k can be fully anisotropic, orthotropic, or isotropic.

2.3. Boundary conditions

Boundary conditions can be specified as prescribed temperature $\boldsymbol{T = T(x,t)}$; prescribed surface heat flux, $\boldsymbol{q = q(x,t)}$ per area; prescribed volumetric heat flux $\boldsymbol{q = r(x,t)}$ per volume; surface convection: $\boldsymbol{q = h(T - T^0)}$, where $\boldsymbol{h = h(x,t)}$ is the film coefficient and $\boldsymbol{T^0 = T^0(x,t)}$ is the sink temperature; and radiation: $\boldsymbol{q = A(T - T^Z)^4 - (T^0 - T^Z)^4}$, where A is the radiation constant (emissivity times the Stefan-Boltzmann constant) and $\boldsymbol{T^Z}$ is the value of absolute zero on the temperature scale being used.

2.4. Spatial discretization

A variational statement of the energy balance, Equation 1, together with the Fourier law, Equation 3, is obtained directly by the standard Galerkin approach as

$$\boldsymbol{\int_V \rho \dot{U} \delta T dV + \int_V \frac{\partial \delta T}{\partial x} k \frac{\partial T}{\partial x} dV = \int_V \delta T r dV + \int_{S_q} \delta T q dS}$$

(3)

where $\boldsymbol{\delta T}$ is an arbitrary variational field satisfying the essential boundary conditions. The body is approximated geometrically with finite elements, so the temperature is interpolated as

$$\boldsymbol{T = N^N(x) T^N, N = 1, 2, ...}$$

where $\boldsymbol{T^N}$ are nodal temperatures. The Galerkin approach assumes that the variational field is interpolated by the same functions:

$$\boldsymbol{\delta T = N^N \delta T^N}$$

with these interpolations, the variational statement (used $\boldsymbol{N^N}$) and since the $\boldsymbol{\delta T^N}$ are arbitrarily chosen, this gives the system of equations:

$$\boldsymbol{\int_V N^N \rho U \dot{d}V + \int_V \frac{\partial N^N}{\partial x} k \frac{\partial T}{\partial x} dV = \int_V N^N r dV + \int_{S_q} N^N q dS} \quad (4)$$

2.5. Time integration

Abaqus/Standard uses the backward difference algorithm:

$$\boldsymbol{\dot{U}_{t+\Delta t} = (U_{t+\Delta t} - U_t)\left(\frac{1}{\Delta t}\right)} \quad (5)$$

This operator is chosen for a number of reasons. First of all, we choose from one-step operators of the form:

$$\boldsymbol{f_{t+\Delta t} = f_t + ((1-\gamma)\dot{f}_t + \gamma \dot{f}_{t+\Delta t})\Delta t}$$

However, that form of the operator tends to produce oscillations in the early - time solution that are not present in the backward difference form. Thus, we use $\boldsymbol{\gamma = 1}$: backward difference. Introducing the operator, Equation 5, into the energy balance Equation 4 gives:

$$\boldsymbol{\frac{1}{\Delta t}\int_V N^N \rho (U_{t+\Delta t} - U_t) dV + \int_V \frac{\partial N^N}{\partial x} k \frac{\partial T}{\partial x} dV - \int_V N^N r dV - \int_{S_q} q dS = 0} \quad (6)$$

This nonlinear system is solved by a modified Newton method. The formation of the terms in this tangent matrix is now described.

The internal energy term gives a Jacobian contribution:

$$\boldsymbol{\frac{1}{\Delta t}\int_V N^N \rho \left.\frac{dU}{dT}\right|_{t+\Delta t} N^M dV}$$

$(\boldsymbol{dU/dT})|_{\boldsymbol{t+\Delta t}}$: is the specific heat, $\boldsymbol{c(T)}$, outside the latent heat range, and is $\boldsymbol{c + L/(T_L - T_S)}$ if $\boldsymbol{T_L > T_{t+\Delta t} > T_S}$at the integration point, where $\boldsymbol{T_L}$ and $\boldsymbol{T_S}$ are the liquidus and solidus temperatures and *L* is the latent heat associated with this phase change.

With film and radiation conditions, the surface flux term gives a Jacobian contribution:

$$\int_S \boldsymbol{N^N} \frac{\boldsymbol{\partial q}}{\boldsymbol{\partial T}}|_{\boldsymbol{t+\Delta t}} \boldsymbol{N^M dS}$$

For film conditions, $\boldsymbol{q = h(T)(T - T^0)}$, $\frac{\boldsymbol{\partial q}}{\boldsymbol{\partial T}} = \frac{\boldsymbol{\partial h}}{\boldsymbol{\partial T}}\boldsymbol{(T - T^0)} + \boldsymbol{h}$

while for radiation, $\boldsymbol{q = A\left(T^4 - T^{0\,4}\right)}$, $\frac{\boldsymbol{\partial q}}{\boldsymbol{\partial T}} = \boldsymbol{4AT^3}$

These terms are included in exactly this form in the Jacobian. The modified Newton method is then:

$$\left[\frac{\boldsymbol{1}}{\boldsymbol{\Delta t}}\int_V \boldsymbol{N^N \rho}\left.\frac{\boldsymbol{dU}}{\boldsymbol{dT}}\right|_{\boldsymbol{t+\Delta t}} \boldsymbol{N^M dV} + \int_V \frac{\boldsymbol{\partial N^N}}{\boldsymbol{\partial x}} \boldsymbol{k}|_{\boldsymbol{t+\Delta t}} \frac{\boldsymbol{\partial N^M}}{\boldsymbol{\partial x}} \boldsymbol{dV} + \int_S \boldsymbol{N^N}\left(\frac{\boldsymbol{\partial h}}{\boldsymbol{\partial T}}\boldsymbol{(T - T^0)} + \boldsymbol{h} + \boldsymbol{4AT^3}\right)\boldsymbol{N^M \partial S}\right]\boldsymbol{c^{-M}}$$
$$= \int_V \boldsymbol{N^N r dV} + \int_S \boldsymbol{N^N q dS} - \frac{\boldsymbol{1}}{\boldsymbol{\Delta t}}\int_V \boldsymbol{N^N \rho(U_{t+\Delta t} - U_t) dV} - \int_V \frac{\boldsymbol{\partial N^N}}{\boldsymbol{\partial x}} \boldsymbol{k} \frac{\boldsymbol{\partial T}}{\boldsymbol{\partial x}} \boldsymbol{dV}$$

with $\boldsymbol{T^N_{t+\Delta t,i+1} = T^N_{t+\Delta t,i} + c^{-N},\ i = iteration\ number}$ (7)

For purely linear systems, Equation 7 is linear in $\boldsymbol{c^{-M}}$ and, hence, in $\boldsymbol{T^N_{t+\Delta t}}$, so a single equation solution provides the $\boldsymbol{T^N_{t+\Delta t}}$. Since the method is usually only a minor modification of Newton's method, convergence is rapid.

3. MODELING AND EXPERIMENTAL

2.1. Modeling and Simulation

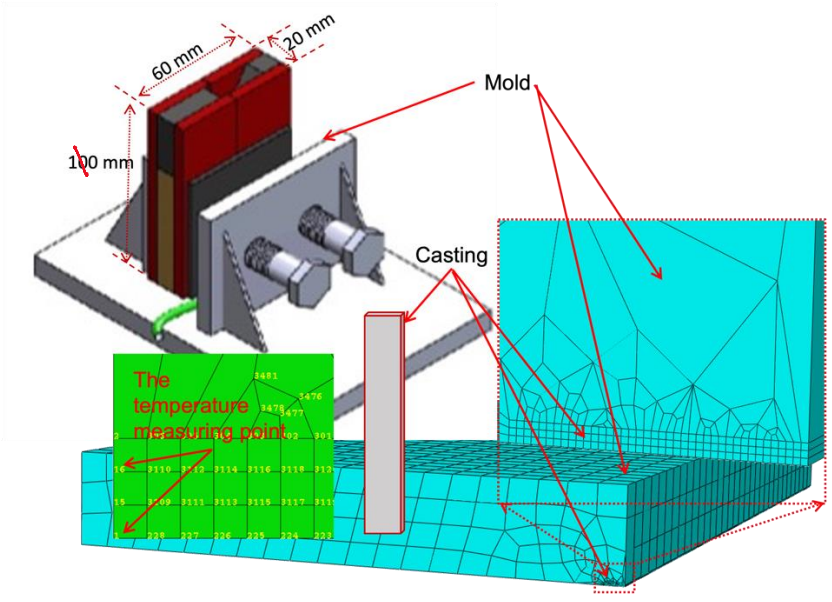

Figure 2. The casting mold system used in experiments and simulations

The casting mold system used in experiments and simulations shown in Figure 2. The mold is made of pure copper material, smoothed flat and polished on all sides, the dimensions are 60 mm in width, 110 mm in height, and 20 mm in thickness. A vacuum system is designed to prevent oxidation and speed up the mold filling of the casting. The castings had a height of 100 mm, with different thicknesses: 0.3, 0.5, 1, 2, 3 and 20 mm.

By using 3D simulation, the developed model calculated and simulated processes with a combination of heat exchange and solid-liquid phase transition. Figure 2 shows the modeling and meshing in the calculation with: 11220, 9512, 8036, 7052, 7093 total number of nodes for: 9450, 7840, 6480, 5600, 5640 elements of heat transfer. The steady conduction solution for this problem was computed.

The initial temperatures of the liquid AlMnCe alloy were 1000 ^{o}C. The contact between the mold and the melt was selected as the film conditions. Data for the thermal-physical properties are presented in Table 1.

Table 1. The thermal-physical properties [31].

Thermal-physical properties	AlMnCe		Mold (Cu)
	Solid	Liquid	
Temperature (^{o}C)	705	730	25
Bulk density (kg/m^3)	2720	2385	8940
Specific heat capacity ($J/kg.K$)	904	108	380
Thermal conductivity ($W/m.K$)	226	105	380
Latent heat (J/kg)		360000	

2.3. Experimental (Microstructure Characterization and Tensile Testing)

In this study, raw AlMnCe materials were used. The samples were dosed according to the atomic ratio of Al92Mn6Ce2 (in atomic percent, at%) and melted in an intermediate frequency induction melting furnace. The mold was designed similarly to the one in the simulation problem. The castings with a height of 100 mm and different thicknesses: (0.5, 1, 2, 3 and 20) mm were fabricated to achieve different cooling rates and to investigate the effect of the cooling rate on the microstructure and mechanical properties.

The polished casting specimens were observed using a HITACHI S-4800 field-emission scanning electron microscopy (SEM) equipped with an X'pert Pro of Malvern Panalytical energy dispersive spectroscope (EDS, EDX) and Digital optical microscopy (VHX-7000).

Moreover, tensile tests were performed on the INSTRON 3382 tensile machines at room temperature using sheet specimens.

3. RESULTS AND DISCUSSION

The temperature data was numerical calculated at the casting with different thicknesses, as shown in Table 2. Figure 3 represents the temperature profile resulted numerical calculated at the casting with different thicknesses varying from 0.3 to 20 mm in the cooling channel. The largest cooling rate found to be about ~10^4 K/s the casting with 0.3, 0.5 and 1 mm thicknesses. With the other thinknesses of 2 and 3 mm, the cooling is slower, with a reduced cooling rate of 10^3 K/s (at the center of the casting) and ~ 10^4 K/s (at the surface of the casting). In the case of a

20 mm thick casting, the cooling rate at the surface is ~ 10^3 *K/s*, the center the cooling rate at the same rate as in conventional die casting (~ 10^2 *K/s*). In particular, the cold line has a thermal arrest, showing the role of latent heat in the solidification process.

Table 2. The temperature data calculated at the casting with different thicknesses.

Time	Near Surface						Center					
	03 mm	**0.5 mm**	**1 mm**	**2 mm**	**3 mm**	**20 mm**	**03 mm**	**0.5 mm**	**1 mm**	**2 mm**	**3 mm**	**20 mm**
0	1000	1000	1000	1000	1000	1000	1000	1000	1000	1000	1000	1000
0.1	45.474	58.261	91.996	151.887	198.612	550.136	46.397	59.490	96.333	165.930	241.781	828.819
0.2	31.815	34.734	43.864	61.041	82.404	487.417	31.793	34.732	43.971	61.959	87.098	748.524
0.3	28.740	30.357	35.360	44.412	56.734	470.789	28.734	30.355	35.371	44.541	57.583	730.799
0.4	27.654	28.848	32.459	38.903	47.835	460.371	27.652	28.847	32.463	38.945	48.129	729.893
0.5	27.146	28.135	31.087	36.335	43.672	452.779	27.145	28.134	31.089	36.356	43.824	729.369
0.6	26.858	27.725	30.298	34.865	41.292	447.161	26.858	27.725	30.299	34.879	41.389	727.735
0.7	26.672	27.457	29.779	33.901	39.728	442.976	26.672	27.457	29.780	33.910	39.799	724.166
0.8	26.540	27.263	29.404	33.204	38.595	439.184	26.540	27.263	29.404	33.211	38.650	716.441
0.9	26.438	27.113	29.114	32.665	37.716	434.742	26.438	27.113	29.114	32.672	37.760	685.240
1	26.356	26.992	28.879	32.229	37.001	427.639	26.356	26.992	28.879	32.234	37.037	616.894

As we know, extremely cool liquid metal turns into an amorphous state when the crystallization process is hindered. Amorphous materials obtained at different cooling rates will have different structures. However, because aluminium is difficult to become amorphous with low GFA (glass forming ability), the cooling speed of about 10^4 *K/s* (cast in vacuum copper die, 0.3 and 0. 5 mm) is still not enough to create amorphous.

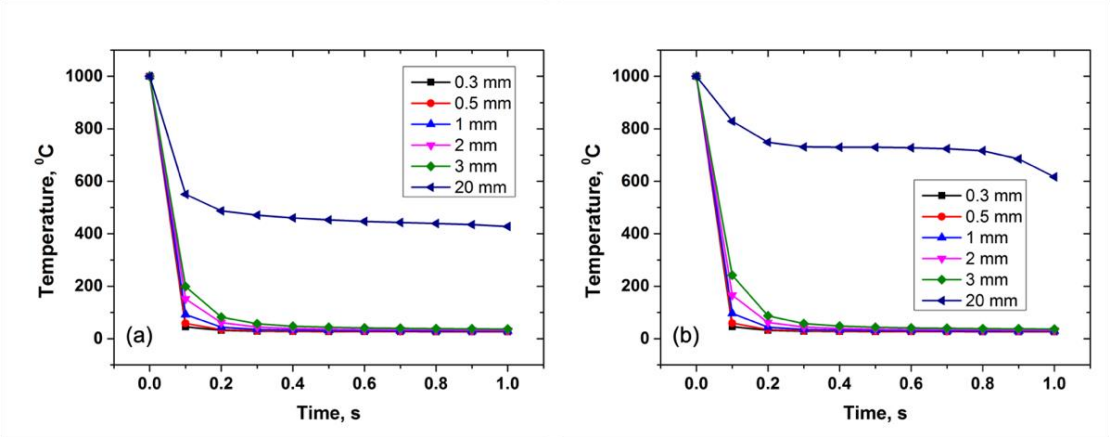

Figure 3. The temperature profile results (a) at near surface and (b) at the center of the casting.

Figure 4 shows the cooling rate curves at the near surface between the casting and center of the as-cast alloys during solidification. We see that the cooling rate is not significantly different with the casting thickness of 0.3, 0.5, 1 mm, a little with a thickness of 2, 3 mm and large with a thickness of 20 mm.

The effect of cooling speed with different thicknesses: 20, 3, 1 and 0.5 mm, corresponds to increasing cooling rates of 10^2, 10^3 and 10^4 K/s, respectively. It can be clearly seen that the secreted intermetallic phases have a decreasing size: when the cooling speed is 10^2 K/s (Figure 7), the intermetallic phase has a rather coarse size (10 - 20 μm) due to its long contact time with liquid metal and favorable conditions for growth. At such a low cooling rate, a phase with a high atomic number, Al8Mn4Ce also known as the "τ" phase) can be formed instead of Al20Mn2Ce since the Mn and Ce atoms diffuse into this phase.

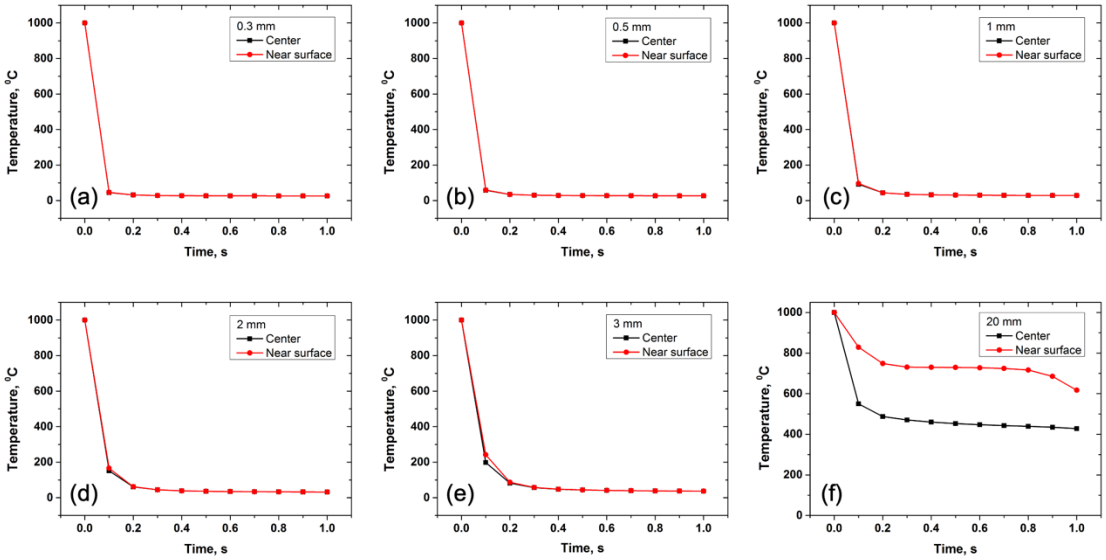

Figure 4. The temperature profile results at near surface and the center for thickness 0.3 mm(a), 0.5 mm(b), 1 mm(c), 2 mm(d) 3 mm(e) and 20 mm (f) of the casting.

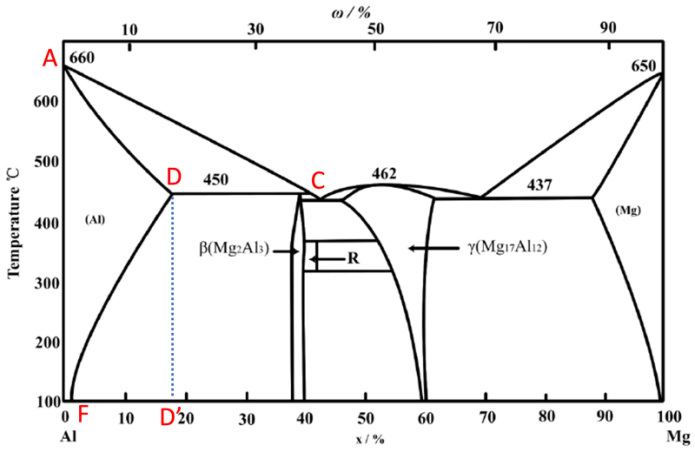

Figure 5. The phase diagram of Al-Mn alloys [31].

When adding alloy elements to aluminium (in liquid state), it often creates an Al - alloy element phase diagram (Figure 5). The alloying element can dissolve in Al to form a solid solution, or, when it exceeds the solubility limit (DF line), it will create a second phase. Based

on the transformation temperature, the inflection points correspond to the formations of α-Al dendrite and eutectic phases, respectively. It is evident that the formation of α-Al occurs first, at the beginning of solidification, while the formation of eutectic phase comes later and the solidification happens at the end.

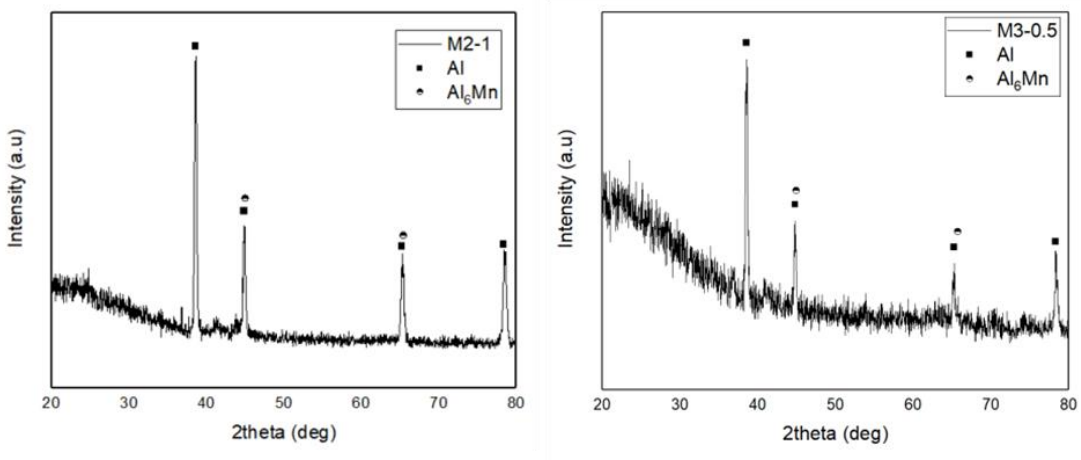

Figure 6. The analysis of *X-ray* diffraction thicknesses: 1 (M2-1) and 0.5 (M3-0.5) mm.

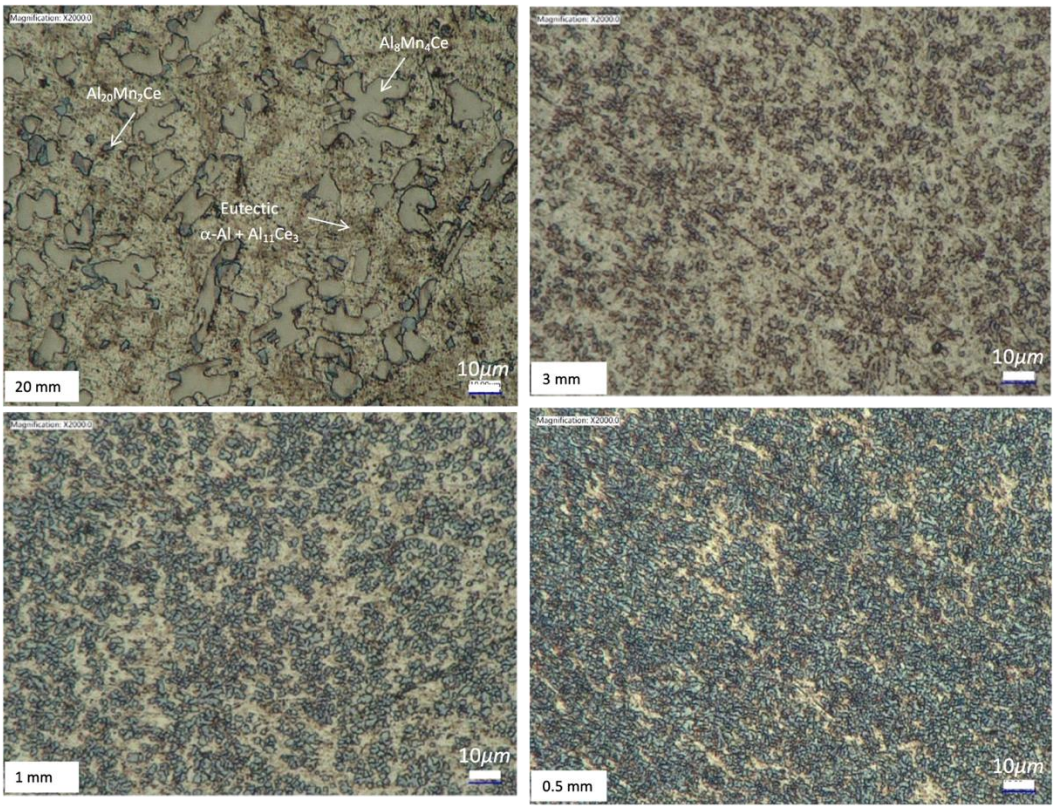

Figure 7. Microscopic organization with different thicknesses (20, 3, 1, 0.5 mm) corresponds to the cooling rate 10^2, 10^3 and 10^4 K/s.

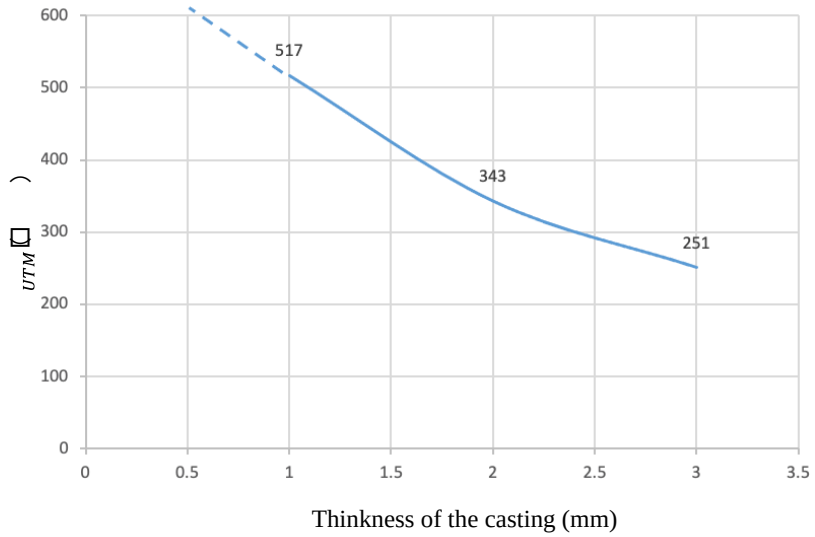

Figure 8. The tensile strength of the casting with different thicknesses.

Figure 6 shows the analysis of *X-ray* diffraction results of Al–Mn–Ce alloy at different cooling rates. It can be seen from Figure 6 that when Al92Mn6Ce2 alloy is prepared using the cast-in metal mold method with thicknesses 1 and 0.5 mm of the casting bar, the main formation phases in the alloy are the Al_6Mn phase and face centered cubic aluminium phase.

The tensile strength of the casting with different thicknesses is shown in Figure 8. Since the 0.5 mm thick samples was small traction for tensile samples, data were not available, the strength of 1 mm thickness of the casting is 517 MPa.

4. CONCLUSIONS

In the paper, by numerical simulation (ABAQUS, FEM) and experimental methods, the cooling rate was investigated by changing the product thickness (0.3, 0.5, 1, 2, 3 and 20 *mm*) to fabricate Al based two-phase nanostructured materials casted through a copper mold. Simulation and Experimental results show that the solidificated ntermetallic phases have a decreasing size corresponding to the increasing cooling rates.

The effect of cooling speed with different thicknesses: 20, 3, 1 and 0.5 *mm*, corresponds to increasing cooling rates of 10^2, 10^3 and 10^4 *K/s*, respectively. It can be easily observed that the secreted intermetallic phases have a decreasing size: when the cooling speed is 10^2 *K/s*, the intermetallic phase has a rather large size (10 - 20 μm) due to its long contact time with liquid metal and favorable conditions for growth.

The strength of 1 *mm* thick casting is 517 *MPa.*

Acknowledgements. Authors are grateful for the support by the **B2022-BKA-16** project funded by the Ministry of Education and Training of Vietnam.

CRediT authorship contribution statement. **Nguyen Hong Hai**: Supervision, Methodology, Investigation, Funding acquisition, Review and Editing. **Le Minh Duc**: Formal analysis, Data curation,

Investigation. **Hoang Thi Ngoc Quyen**: Formal analysis, Investigation. **Pham Quang**: Writing - Original Draft, Data analysis, Methodology, Review and Editing.

Declaration of competing interest. The authors declare that they have no known competing financial interests or personal relationships that could have appeared to influence the work reported in this paper.

REFERENCES

1. Shin S., Yeom G., Kwak T., Park I. – Microstructure and mechanical properties of TiB-containing Al-Zn binary alloys, J. Mater. Sci. Technol. **32** (2016) 653-659. DOI: 10.1016/j.jmst.2016.04.016.
2. Shin S., Lim K., Park I. - Characteristics and microstructure of newly designed Al-Zn-based alloys for the die-casting process, J. Alloy. Comp. **671** (2016) 517-526. https://doi.org/10.1016/j.jallcom.2016.02.127.
3. Guo H., Yang X., Wang J., Hu B., Zhu G. - Effects of rheoforming on micro structures and mechanical properties of 7075 wrought aluminium alloy, T. Nonferr. Metal Soc. **20** (2010) 355-360. https://doi.org/10.1016/S1003-6326(09)60146-1.
4. Duc D. M., Hai N. H., and Quang P. - Modeling of continuous rheo-casting the A356 alloy by finite element method (FEM), Sci. Tech. Metals **46**, 37 (2013).
5. Tai N. T., Duc D. M., Hai N. H., and Quang P. - Optimization of flow behavior in high-pressure die casting by the Pro/Engineer virtual manufacturing, J. of Science and Technology **5A** (201) (2013).
6. Tai N. T., Duc D. M., Hai N. H., and Quang P. - Effect of pressure on microstructure and mechanical properties of A356 aluminium alloy during rheo-diecasting process (RDC), J. of Science and Technology **5A** (194) (2013).
7. Duc D. M., Hai N. H., and Quang P. - Simulation and experimental study on the steady conduction solution for continuous rheo-casting for A356 alloy, Korean J. Met. Mater. **55** (3) (2017), 202-208. https://doi.org/10.3365/KJMM.2017.55.3.202
8. Nguyen Hong Hai, Pham Quang - Effect of Pressure on Solidification Process and Mechanical Properties During Semi-Solid Casting by Computational Fluid Dynamics (CFD). Advances in Materials. **7** (2) (2018) 44-49. doi: 10.11648/j.am.20180702.15.
9. Górny M., Tyrała E. - Effect of Cooling Rate on Microstructure and Mechanical Properties of Thin-Walled Ductile Iron Castings. J. of Materi Eng and Perform. **22** (2013) 300–305. https://doi.org/10.1007/s11665-012-0233-0.
10. Tang H. P. et al. - Effect of cooling rate on microstructure and mechanical properties of an Al-5.0Mg-3.0Zn-1.0Cu cast alloy, Journal of Alloys and Compounds, **801** (2019) 596-608. https://doi.org/10.1016/j.jallcom.2019.06.002.
11. Juan W. *et al*. - Effect of cooling rate on the microstructure and thermal expansion properties of Al–Mn–Fe alloy, Reviews on Advanced Materials Science. **61** (2022) 265–275. https://doi.org/10.1515/rams-2022-0031.
12. Zare M. A., Taghiabadi R. & Ghoncheh M. H. - Effect of Cooling Rate on Microstructure and Mechanical Properties of AA5056 Al-Mg Alloy. Inter Metalcast. **16** (2022) 1533–1543. https://doi.org/10.1007/s40962-021-00704-6.
13. Tsai A. P., Inoue A. and Masumoto T. - A stable quasicrystal in Al–Cu–Fe System. Japanese Journal of Applied Physics. **26** (9A) (1987), id. L1505.

14. Yadav T. P. and Mukhopadhyay N. K. - Quasicrystal: A low-frictional novel material. Chemical Engineering. **19** (2018) 163–169. https://doi.org/10.1016/j.coche.2018.03.005.
15. Galano M., Audebert F., Escorial A. G., Stone I. C. and Cantor B. - Nanoquasicrystalline Al–Fe–Cr-based alloys with high strength at elevated temperature. Journal of Alloys and Compounds. **495** (2) (2010) 372–376. https://doi.org/10.1016/j.jallcom.2009.10.208.
16. Zupanič F., Bončina T., Križman A., Grogger W., Gspan C., Markoli B., et al. - Quasicrystalline phase in melt-spun Al–Mn–Be ribbons. Journal of Alloys & Compounds. **452** (2) (2008) 343–347. https://doi.org/10.1016/j.jallcom.2006.11.041.
17. Inoue A., Watanabe M., Kimura H. M., Takahashi F., Nagata A. and Masumoto T. - High mechanical strength of quasicrystalline phase surrounded by fcc-Al phase in rapidly solidified Al–Mn–Ce alloys. Materials Transactions, JIM. **33** (1992) 723–729. https://doi.org/10.2320/matertrans1989.33.723.
18. Chang H. J., Fleury E., Song G. S., Lee M. H., Kim W. T. and Kim D. H. - Microstructure modification and quasicrystalline phase formation in Al–Mn–Si–Be cast alloys. Materials Science & Engineering A. **375** (377) (2004) 992–997. https://doi.org/ 10.1016/j.msea.2003.10.004.
19. Chang H. J., Fleury E., Song G. S., Kim W. T. and Kim D. H. - Formation of quasicrystalline phases in Al-rich Al–Mn–Be alloys. Journal of Non-Crystalline Solids. **334** (2004) 12–16. https://doi.org/10.1016/j.jnoncrysol.2003.11.005.
20. Zupanic F., Boncina T., Rozman N., Anzel I., Grogger W., Gspan C., et al. Development of an Al–Mn–Be–Cu alloy with improved quasicrystalline forming ability. International Journal for Structural Physical & Chemical Aspects of Crystalline Materials. **223** (11–12) (2008) 735–738. https://doi.org/10.1524/zkri.2008.1037.
21. Eisenbud M., Kotin P., and Miller F. - Is beryllium carcinogenic in humans? Journal of Occupational & Environmental Medicine. **39** (3) (1997) 205–208.
22. Schurack F., Eckert J., and Schultz L. - Synthesis and mechanical properties of cast quasicrystal-reinforced Al- alloys. Acta Materialia. **49** (8) (2001) 1351–1361. https://doi.org/10.1016/S1359-6454(01)00045-3.
23. Coury F. G., Botta W. J., Bolfarini C., Kiminami C. S. and Kaufman M. J. - Reassessment of the effects of Ce on quasicrystal formation and microstructural evolution in rapidly solidified Al–Mn alloys. Acta Materialia. **98** (2015) 221–228. https://doi.org/10.1016/j.actamat.2015.07.046.
24. Stan K., Lityńska-Dobrzyńska. L., Dutkiewicz J., Rogal L., and Janus A. M. - TEM study of quasicrystals in Al–Mn–Fe melt-spun ribbon. Solid State Phenomena. **186** (2012) 255–258. DOI:10.4028/www.scientific.net/SSP.186.255.
25. Stan K., Lityńska-Dobrzyńska L., Lábár J. L., and Góral A. - Effect of Mo on stability of quasicrystalline phase in Al–Mn–Fe alloy. Journal of Alloys and Compounds. **586** (2014) 395–399. https://doi.org/10.1016/j.jallcom.2012.12.013.
26. Stan-Głowińska K., Lityńska-Dobrzyńska L., Kania B., Dutkiewicz J., Skuza W., Wojewoda-Budka J., *et al*. - Effects of hot-compaction on the structure and properties of AlMn-Fe-X alloys strengthened with quasi-crystalline icosahedral phase. Materials & Design. **126** (2017) 162–173. https://doi.org/10.1016/j.matdes.2017.04.043.

27. Stan-Głowińska K. and Lityńska-Dobrzyńska L. - Influence of Fe addition on the formation of a quasicrystalline phase in bulk Al-rich Al-Mn base alloys. Materials Characterization. **128** (2017) 203–208. https://doi.org/10.1016/j.matchar.2017.04.006.
28. Balanetskyy S., Pavlyuchkov D., Velikanova T., and Grushko B., The Al-rich region of the Al-Fe-Mn alloy system. Journal of Alloys and Compounds. **619** (2014) 211–220. https://doi.org/10.1016/j.jallcom.2014.08.232.
29. Abaqus/CAE User's Guide: Abaqus 6.14, © Dassault Systèmes, 2011.
30. Abaqus/Theory Manual: Uncoupled heat transfer analysis, © Dassault Systèmes, 2011.
31. Brandes E. A., Smithells Metals Reference Book (Seventh Edition) Published by Butterworth & Co. Ltd (1983).